Predictive modeling and optimization of surface roughness in LPBF through artificial neural networks

The International Journal of Advanced Manufacturing Technology (2026) 143:1995–2015
https://doi.org/10.1007/s00170-025-17122-1

ORIGINAL ARTICLE

Predictive modeling and optimization of surface roughness in LPBF through artificial neural networks

Delio Lusicini[1] · Matteo Crachi[1] · Raffaella Sesana[1] · Cristiana Delprete[1] · Marco Pizzarelli[2] · Nicola Sicignano[3] · Domenico Borrelli[3] · Antonio Caraviello[3]

Received: 21 June 2025 / Accepted: 25 November 2025 / Published online: 5 January 2026

Abstract

In this study, experimental measurements of surface roughness were conducted on samples produced using Laser Powder Bed Fusion, with particular attention to the influence of scanning speed and laser power in both the body and contour regions. The roughness was evaluated at different heights within the build volume and across multiple surface orientations relative to the recoater blade. Based on the collected data, a feedforward Artificial Neural Network was trained using process parameters and geometrical factors (height and angle) as input, and experimentally measured roughness as output. The trained model achieved high predictive accuracy, with a Pearson correlation coefficient of 0.92 between predicted and measured values. Using the predictive capabilities of the Artificial Neural Network, it was possible to identify optimized combinations of process parameters for each combination of height and angle within the build volume. The optimization led to a significant reduction in surface roughness, lowering the minimum measured *Ra* (at Height = 15mm and Angle = 180°) from 5.51µm (experimentally obtained) to a predicted 3.46µm under the optimal parameter configuration, and achieving an average reduction of approximately 19.4% across the other positions.

Keywords Artificial neural networks (ANNs) · Additive manufacturing (AM) · Roughness · Laser powder bed fusion (LPBF) · Metal matrix composite (MMC) · Machine learning (ML)

1 Introduction

Laser Powder Bed Fusion (LPBF), a prominent additive manufacturing technique, offers design flexibility and ability to produce complex geometries directly from digital models. However, surface quality remains a critical challenge that influences mechanical performance, fatigue life, and post-processing requirements of LPBF parts. Among the various surface features, surface roughness has garnered significant research attention due to its implications for dimensional accuracy, mechanical properties, and functional performance.

The formation of surface roughness in LPBF is intrinsically linked to a multitude of process parameters, including laser power, scanning speed, hatch distance, layer thickness, and powder characteristics. As laser energy interacts with the powder bed, complex thermal and fluid dynamic phenomena emerge, such as Marangoni convection, recoil pressure, melt pool instability, and balling effect, all of which contribute to the resultant surface texture [1]. Higher laser powers generally flatten the melt pool and enhance wettability, thereby reducing both top and side roughness [2]. Conversely, insufficient energy input or overly rapid scanning can induce poor fusion and irregular melt pool geometries, leading to rough and porous surfaces [3].

Furthermore, the role of powder layer thickness and particle morphology is relevant. Thick powder layers or poorly packed powders exacerbate porosity and increase the effective roughness due to incomplete melting and stair-stepping effects [4]. Surface roughness is also anisotropic (typically lower on the top surfaces compared to the sides) due to

✉ Delio Lusicini
delio.lusicini@polito.it

[1] DIMEAS, Politecnico di Torino, Corso Duca degli Abbruzzi 24, 10129 Turin, Italy

[2] Agenzia Spaziale Italiana, Via del Politecnico, 00133 Rome, Italy

[3] Sophia High Tech s.r.l., Via Malatesta 30A, 80049 Somma Vesuviana, Italy

differences in thermal gradients and solidification conditions during layer-by-layer construction [5].

Beyond experimental observations, computational fluid dynamics (CFD) and volume of fluid (VoF) simulations have explained the transient behaviors of melt pool dynamics and surface formation, offering valuable insights into parameter optimization strategies [1]. Research efforts are increasingly focused on multiscale modeling, adaptive process control, and hybrid manufacturing strategies. Continued exploration of the interplay between process parameters and surface morphology is crucial for advancing LPBF towards more reliable and ready for application production technologies [6].

Machine learning (ML) has emerged as a key enabler for addressing the challenges associated with metal additive manufacturing (AM), such as process complexity, material development, post-processing, and quality consistency [7]. By analyzing complex relationships between process parameters and material responses, ML supports the prediction of key mechanical properties, such as tensile strength, yield strength, and fatigue resistance–and enables optimization of both printing and post-processing conditions [8–11]. This leads to reduced experimental efforts, improved component quality, and accelerated industrial implementation of AM.

Among the most commonly used ML methods are regression analysis, artificial neural networks (ANNs), support vector machines (SVM), genetic algorithms, reinforcement learning, decision trees, and Bayesian approaches [10, 12]. Their integration into AM typically follows a structured workflow, starting from data collection and preprocessing, followed by model selection, training, validation, and deployment for real-time monitoring, adaptive control, and predictive maintenance [13, 14].

Particularly, ANNs have proven effective in capturing nonlinear interactions in complex manufacturing processes, enabling accurate property prediction and process parameter optimization [15, 16]. Feedforward neural networks (FNNs) are frequently employed for these tasks, where data flows from the input to the output layer through hidden layers, allowing the network to learn functional dependencies without requiring explicit physical models. Model performance depends on architecture, activation functions, training algorithms, and data quality [16, 17]. Establishing the optimal configuration of these factors for a ANN remains a challenging task [17]. One of the most critical challenges in training ANNs is the risk of overfitting, a phenomenon where the model performs extremely well on the training data but fails to generalize to unseen data. Overfitting typically arises when the model has too many parameters relative to the amount of training data, enabling it to memorize noise and spurious correlations instead of learning the underlying functional relationships [15, 18] .

In recent years, surface roughness prediction in additive manufacturing (AM) has received growing attention, particularly through the integration of machine learning and deep learning (DL) techniques. Batu et al. [19] presented a comprehensive review of AI approaches for surface roughness prediction in AM, highlighting the superiority of ML models over conventional statistical methods due to their ability to handle nonlinear relationships and large datasets. Muhammad et al. [20] developed a deep learning framework for predicting the surface roughness of LPBF AlSi10Mg specimens, achieving high accuracy with errors below 5% when compared to experimental measurements. Their approach accounted for both process parameters (laser power, scanning speed, and layer thickness) and geometric location. Alamri et al. [21] compared five ML algorithms (artificial neural networks, support vector regression (SVR), kernel ridge regression (KRR), random forest (RF), and Lasso regression) for predicting porosity, hardness, and surface roughness in LPBF AlSi10Mg alloys, demonstrating that ANN and RF provided the most accurate results. Koo et al. [22] proposed a predictive framework based on SVR, RF, and multilayer perceptron (MLP) models to estimate downskin roughness in CM247LC components, using input variables such as laser power, scanning speed, hatching distance, and overhang angle, and achieving a coefficient of determination $R^2 = 0.93\%$. Similarly, Islahudin et al. [23] developed an ML driven optimization model for Ti6Al4V, achieving $R^2 = 0.97\%$ and a mean squared error of 0.1383, thereby demonstrating that ML based frameworks can effectively support surface quality prediction and optimization in AM processes.

1.1 Aims

Surface roughness in LPBF is strongly affected by key process parameters, particularly laser power, scanning speed, and hatch distance, which together define the energy density [24–29]. Higher laser power generally reduces roughness by stabilizing the melt pool and improving layer bonding, while excessive power may cause defects such as porosity [30]. Scanning speed plays a dual role: lower speeds enhance melting and surface smoothness, whereas higher speeds increase roughness due to incomplete fusion or spattering [24, 31]. Hatch distance also critically influences roughness; smaller values improve track overlap but may cause heat accumulation, while larger ones reduce overlap and prevent excessive remelting [32]. Optimizing energy density is therefore essential to ensure stable melt pool behavior and minimize surface defects [27]. Although results vary across studies due to differences in materials and conditions, achieving balanced laser parameters

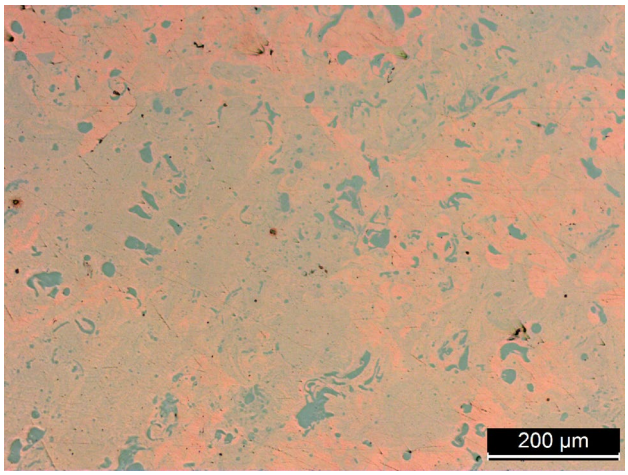

Fig. 1 Cu174PH8020 metal matrix composite micrography with respect to plane xy

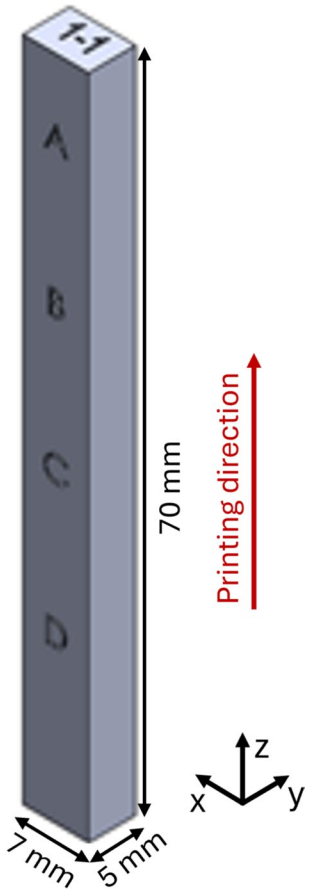

Fig. 2 Geometry of the prismatic specimens used for surface roughness measurements

remains key to minimizing roughness in copper and copper alloy LPBF systems [29, 33]. Thermal gradients along the build height could affect microstructure and residual stress, leading to variations in surface roughness at higher levels [34, 35]. Additionally, the angular orientation relative to the recoater blade could affect local powder distribution, influencing surface roughness uniformity.

Building on these findings, the present study aims to predict the effect of processing parameters on the surface roughness of Cu174PH8020 specimens manufactured by LPBF. Specifically, the effects of the body laser power (LPb), body scanning speed (SSb), contour laser power (LPc), contour scanning speed (SSc), together with the geometrical factors of build angle and height, were analyzed along with their interactions. In particular, an ANN will be trained using data obtained from surface roughness measurements. Several model architectures will be tested, and the trained network will then be used to identify process parameter combinations, outside the scope of those physically tested, that are expected to minimize surface roughness.

The remainder of this paper is structured as follows:

- Section 2 describes the materials and methods applied in the experimental campaign, including the manufacturing parameters and data acquisition procedures.
- Section 3 presents and discusses the main results, highlighting the predictive performance of the neural network model and the optimization outcomes.
- Section 4 provides the conclusions and outlines future developments.
- Publisher's Note, Funding, and Declarations reports, including author contributions and acknowledgments.

2 Materials and methods

The material investigated in this study is Cu174PH8020, which was fabricated mixing 80% of pure copper and 20% of 17-4 PH maraging steel. The process involved to manufacture the specimens is the additive LPBF process. The production of the samples was carried out using a Concept Laser M2 machine equipped with a red laser. The resulting material can be classified as a metal matrix composite, featuring a copper matrix embedded with discrete islands of 17-4 PH steel. In addition to these distinct phases, intermediate regions characterized by partial mixing of the two constituents were also observed. An example of a representative micrograph is shown in Fig. 1, acquired from the *xy* plane of a a specimen manufactured using the following process parameters: LPb = 280W, SSb = 800mm/s, LPc = 180W, and SSc = 400mm/s.

A total of 48 prismatic specimens were produced, each fabricated with a distinct set of process parameters.The specimens are prismatic with a base of 5 mm × 7 mm and a height of 70 mm (Fig. 2).

Specifically, the laser power and scanning speed were systematically varied for both the contour and the body

Table 1 Process parameters for each specimen

ID	Body Parameters		Contour Parameters		ID	Body Parameters		Contour Parameters	
	LP	SS	LP	SS		LP	SS	LP	SS
	[W]	[mm/s]	[W]	[mm/s]	[W]	[mm/s]	[W]	[mm/s]	
1.1			140	300	5.1			140	300
1.2			180	300	5.2			180	300
1.3			180	400	5.3			180	400
1.4	220	800	180	500	5.4	250	900	180	500
1.5			220	400	5.5			220	400
1.6			220	500	5.6			220	500
2.1			140	300	6.1			140	300
2.2			180	300	6.2			180	300
2.3			180	400	6.3			180	400
2.4	250	800	180	500	6.4	280	900	180	500
2.5			220	400	6.5			220	400
2.6			220	500	6.6			220	500
3.1			140	300	7.1			140	300
3.2			180	300	7.2			180	300
3.3			180	400	7.3			180	400
3.4	280	800	180	500	7.4	250	1000	180	500
3.5			220	400	7.5			220	400
3.6			220	500	7.6			220	500
4.1			140	300	8.1			140	300
4.2			180	300	8.2			180	300
4.3			180	400	8.3			180	400
4.4	220	900	180	500	8.4	280	1000	180	500
4.5			220	400	8.5			220	400
4.6			220	500	8.6			220	500

Table 2 Constant parameters

Fusion strategy	Island (5 mm length)
Layer thickness [mm]	0,03
Hatch distance [mm]	0,105
Spot size [mm]	0,15
Overlap factor (body) [-]	0,7
Beam compensation (contour) [mm]	0,075

regions of the samples. This was done to assess the influence of each parameter on surface roughness as well as their interaction effects. This experimental design resulted in 8 different combinations of body parameters and 6 distinct combinations of contour parameters , leading to a total of 48 process parameter sets (see Table 1) used for the specimen production. For completeness, the process parameters held constant across all specimens are summarized in Table 2. The process parameters were carefully selected based on prior knowledge of the LPBF process on similar materials [36, 37], in order to cover a representative range of processing conditions while maintaining experimental feasibility. In Fig. 3, the printing platform is shown, the specimens of interest are highlighted with a red dashed line (Fig. 3 right). The remaining geometries visible on the printing platform were produced as part of a broader experimental campaign

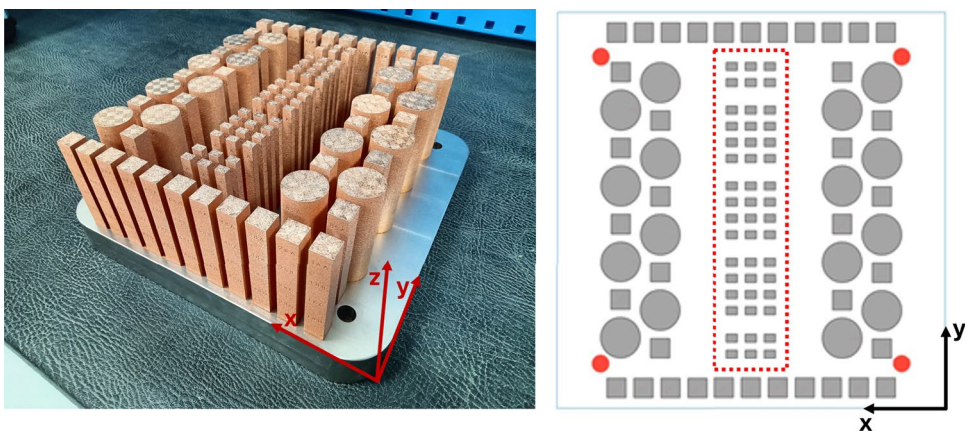

Fig. 3 Photo (on the left) and 2D representation (on the right) of the samples used in this study

and were used in a separate study focused on the characterization of hardness, thermal conductivity, porosity, and microstructural analysis [38].

From [38], no significant variations in material properties were observed across different regions of the build volume; therefore, surface roughness was assumed to remain consistent throughout the printing volume in this study.

Figure 4 presents a schematic illustration of the methodology adopted in this study, which integrates an Artificial Neural Network (ANN) model with a systematic sequential model adjustment and evaluation procedure. The workflow includes a sequential model adjustment to ensure the identification of the best-performing predictive model for Ra estimation.

The methodology can be summarized as follows:

- **Dataset collection:** Experimental data were gathered from printed samples considering different process parameters and geometrical configurations.
- **Data normalization:** All input and output variables were scaled to improve ANN training efficiency.
- **Dataset partitioning:** The dataset was divided into training, validation, and testing subsets to assess model generalization.
- **Initial ANN training:** A base ANN model was trained to establish a preliminary performance benchmark.
- **Sequential model adjustment:** The ANN model was refined through:
  - Variation of the training algorithm;
  - Adjustment of the number of neurons and hidden layers;
  - Selection of different activation functions.
- After each step, models were evaluated using statistical performance metrics, and the *optimal configuration* was selected.
- **Sensitivity analysis:** Conducted to evaluate the influence of each input variable on the predicted surface roughness.
- **Ra minimization:** The trained ANN was used to identify the optimal set of process parameters for minimizing surface roughness.

This sequential approach was selected because it allows clearer interpretation of the influence of each hyperparameter on model performance and helps avoid excessive computational cost associated with exhaustive search or automated optimization algorithms. The adopted strategy was deemed appropriate for this study since it ensures good performance while maintaining transparency and interpretability of the process.

2.1 Experimental setup and physical results

Roughness measurements were performed using a tactile linear RPT-80 roughness-meter. Specifically, for each of the 48 samples, measurements were conducted at three different heights and for three different orientations (Fig. 5), resulting in a total of 432 distinct surface roughness values. Specifically, each surface roughness measurement was repeated three times, and for the purposes of this study, the average of the three values was considered as the reference measurement.

A convention was adopted to define the measurement points based on height and angular orientation.

Specifically, three different heights were considered along the vertical direction of the sample (z build direction), corresponding to:

- 15 mm for the lowest region (closest to the base);
- 35 mm for the middle region;
- 55 mm for the upper region (farthest from the base).

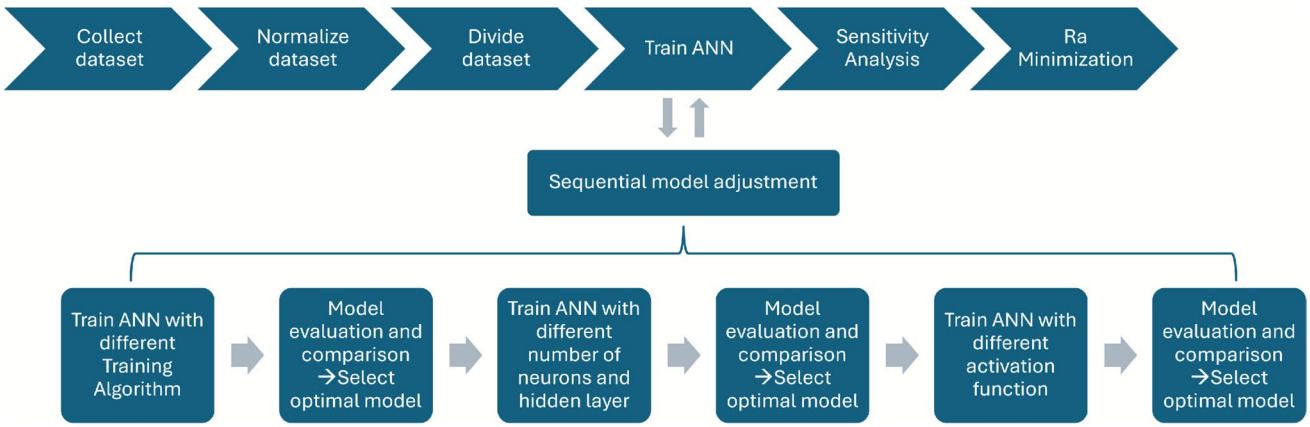

Fig. 4 Schematic illustration of the methodology adopted in this study

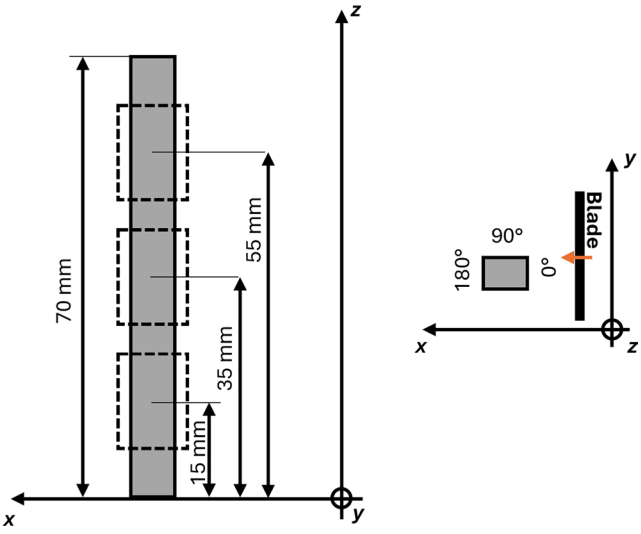

Fig. 5 Schematic representation of the experimental setup, showing the measured area with respect to height and the orientation of the samples' faces

In terms of angular orientation around the specimen perimeter (in the *xy* plane), three reference angles were used:

- 0°, aligned with the blade movement direction;
- 90°, perpendicular to the blade movement direction;
- 180°, opposite to the 0°reference.

All physical measurements are reported in Appendix A, Table 11.

2.2 Predictive modeling using ANNs

In this study, a feedforward ANN was implemented using MATLAB `fitnet` [39] function to predict surface roughness (*Ra*) based on six of the parameters (LP, SS of body and contour, angle and height).

To improve training efficiency and numerical stability, input and target data were normalized using MATLAB `mapminmax` function [40]. This function performs a linear transformation that maps the original data into the interval $[-1, 1]$, using the following formula [40]:

$$y = (y_{\max} - y_{\min}) \cdot \frac{x - x_{\min}}{x_{\max} - x_{\min}} + y_{\min} \quad (1)$$

where:

- x is the original input value,
- $x_{\min}$ and $x_{\max}$ are respectively the minimum and maximum values of the input data,
- y is the normalized output value,
- $y_{\min}$ and $y_{\max}$ are the lower and upper bounds of the normalized output range.

The reason for normalizing the data is that, in a classification task, different attributes may span vastly different numerical ranges. Attributes with larger ranges can disproportionately influence the model's output, not because they are more relevant, but simply due to their higher magnitude of values [41]. Min–Max normalization is a widely recognized technique for preprocessing input data in feedforward artificial neural networks. Chepino et al. [42] demonstrated a significant improvement in classification accuracy (up to 25%) when applying Min–Max normalization compared to using raw data. Similarly, Nawi et al. [43] found that this normalization technique leads to faster model convergence and better overall performance than other preprocessing methods such as Z-score and median normalization across multiple benchmark datasets. According to Sinsomboonthong [41], eight normalization techniques were systematically compared across six benchmark datasets to evaluate their influence on artificial neural network performance. The investigated methods included Min–Max, Z-score, Decimal Scaling, Statistical Column, Adjusted-1 Min–Max, Adjusted-2 Min–Max, Modified, and Column normalization. Among these, the Min–Max method achieved the highest mean classification accuracy (84.0%) and the lowest mean squared error (MSE = 0.1097), demonstrating its superior performance and stability in ANN-based learning tasks.

After prediction, the network output was de-normalized using the inverse transformation. This ensures that the predicted values are converted back to the original scale of the target data. The available dataset was randomly partitioned into three subsets: 75% for training, 15% for validation, and 15% for testing. This division ensures that the model is trained on the majority of the data, while validation is used to monitor generalization performance and prevent overfitting, and the test set is reserved for final performance evaluation.

2.2.1 Network architecture

A sequential model adjustment approach was adopted for the development of the ANN model. Initially, a feedforward ANN with a single hidden layer comprising 10 neurons was constructed. The activation function applied to each hidden neuron was the default hyperbolic tangent sigmoid function (tansig) , defined as [44]:

$$\tanh(x) = 2 \cdot \left(\frac{1}{1 + e^{-2x}} \right) - 1 \quad (2)$$

This nonlinear activation introduces the capacity to model complex, nonlinear relationships within the input data. The output layer employed a linear activation function (purelin) [45]:

$$f(x) = px \tag{3}$$

where p is the hyperparameter. It is appropriate for continuous regression tasks, allowing the network to produce outputs with real value.

The operation of the network can be mathematically described as follows [46]:

$$\mathrm{h} = f^{(1)}\left(\mathrm{W}^{(1)} \cdot \mathrm{x} + \mathrm{b}^{(1)}\right) \tag{4}$$

$$\hat{y} = \mathrm{W}^{(2)} \cdot \mathrm{h} + \mathrm{b}^{(2)} \tag{5}$$

where x is the input vector, h is the hidden layer output, $\mathrm{W}^{(i)}$ and $\mathrm{b}^{(i)}$ are the weight matrices and bias vectors for layer i, and $f^{(1)}$ is the activation function of the hidden neurons.

In addition to tansig, the effect of using the logarithmic sigmoid activation function (logsig) was also evaluated on the best performing architecture. The logsig function is defined as [44]:

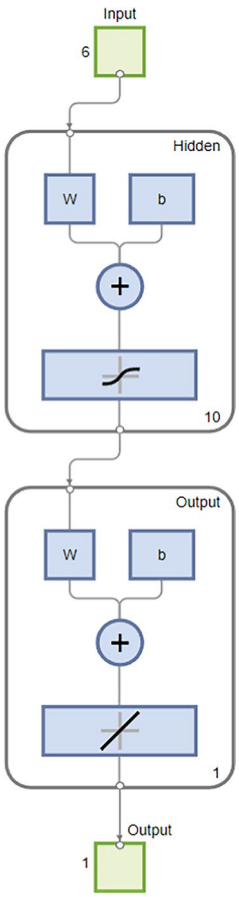

Fig. 6 Initial network diagram representing the baseline architecture used for sequential model adjustment

$$\mathrm{logsig}(x) = \frac{1}{1 + e^{-x}} \tag{6}$$

The maximum number of training epochs was set to 1000, ensuring sufficient iterations for convergence of the learning algorithm.

Figure 6. shows the network diagram of the baseline configuration used in the first step of the sequential model adjustment process.

The learning process was guided by the minimization of the *Mean Squared Error (MSE)* loss function, defined as [47]:

$$\mathrm{MSE} = \frac{1}{n}\sum_{i=1}^{n}(y_i - \hat{y}_i)^2 \tag{7}$$

where y_i is the true target value, $\hat{y}_i$ is the network's prediction, and n is the total number of samples.

The MSE penalizes larger errors more heavily and provides a smooth, differentiable loss landscape, making it suitable for gradient based optimization methods.

2.2.2 Training algorithm

Based on the initial architecture, A range of training algorithms were implemented and evaluated, and the one achieving the best performance was selected for further analysis. The algorithms employed are:

1. Levenberg-Marquardt (trainlm) [48–50];
2. Bayesian Regularization (trainbr) [50–52];
3. BFGS (Broyden–Fletcher–Goldfarb–Shanno) Quasi-Newton (trainbfg) [53, 54];
4. Resilient Backpropagation (trainrp) [55, 56]
5. Scaled Conjugate Gradient (trainscg) [50, 57]
6. Conjugate Gradient with Powell/Beale Restarts (traincgb) [58];
7. Fletcher-Powell Conjugate Gradient (traincgf) [59];
8. Polak-Ribiére Conjugate Gradient (traincgp) [60];
9. One Step Secant (trainoss) [61, 62];
10. Variable Learning Rate Gradient Descent (traingdx) [63, 64];
11. Gradient Descent with Momentum (traingdm) [65, 66];
12. Gradient Descent (traingd) [67, 68].

Once the optimal training algorithm was identified, further experiments were conducted to assess the influence of architectural variations. In particular, the effect of changing the number of neurons in the hidden layer, as well as adding additional hidden layers, was systematically investigated.

Several network configurations were implemented by varying the number of neurons and the depth of the architecture. The goal was to explore the model capacity to capture complex data patterns while evaluating the trade-off between accuracy and computational complexity.

Table 3 lists the parameters used to define the ANN architecture, including the number of neurons, hidden layers, activation functions, and optimization algorithms, all of which were considered as variable during the evaluation process.

2.2.3 Model evaluation and comparison

Each configuration was trained under the same data partitioning and training conditions, and its performance was evaluated using the following regression metrics:

Mean Squared Error (MSE) *Measures the average squared difference between observed and predicted values [69, 70] (defined by Eq. 7).*

Root Mean Squared Error (RMSE) *Square root of the MSE, providing an error measure in the same units as the output [71, 72]:*

$$RMSE = \sqrt{\frac{1}{N}\sum_{i=1}^{N}(y_i - \hat{y}_i)^2} \tag{8}$$

Mean Absolute Error (MAE) *Average of the absolute differences between predictions and actual values [71, 72]:*

$$MAE = \frac{1}{N}\sum_{i=1}^{N}|y_i - \hat{y}_i| \tag{9}$$

Table 3 Initial set of tunable parameters for ANN configuration

Parameter	Value
Number of hidden layers	1 - 3
Neurons in the hidden layers	10 - 30
Activation function (hidden layer)	tansig or logsig
Activation function (output layer)	Linear (purelin)
Maximum number of training epochs	1000
Data set partition	70% training 15% validation 15% test
Loss function	Mean Squared Error (MSE)
Training algorithm	Variable
Maximum number of validation failures	2

Coefficient of Determination (R^2)

Indicates the proportion of variance in the dependent variable that is predictable from the independent variables [71, 72]:

$$R^2 = 1 - \frac{\sum_{i=1}^{N}(y_i - \hat{y}_i)^2}{\sum_{i=1}^{N}(y_i - \bar{y})^2} \tag{10}$$

Pearson Correlation Coefficient (r) *Measures the linear correlation between the predicted and actual values. A value close to +1 or -1 indicates a strong linear relationship between the variables [73]:*

$$r = \frac{cov(y, \hat{y})}{\sigma_y \cdot \sigma_{\hat{y}}} = \frac{\sum_{i=1}^{n}(y_i - \bar{y})(\hat{y}_i - \bar{\hat{y}})}{\sqrt{\sum_{i=1}^{n}(y_i - \bar{y})^2}\sqrt{\sum_{i=1}^{n}(\hat{y}_i - \bar{\hat{y}})^2}} \tag{11}$$

where y are the observed values, $\hat{y}$ are the predicted values, σ_y is the standard deviation of the observed values, $\sigma_{\hat{y}}$ is the standard deviation of the predicted values, $cov(y, \hat{y})$ is the covariance between the observed and predicted values, y_i is the observed value at the i-th observation, $\hat{y}_i$ is the predicted value at the i-th observation, $\bar{y}$ is the mean of the observed values, and $\bar{\hat{y}}$ is the mean of the predicted values.

These metrics provided a comprehensive evaluation of the predictive accuracy, error magnitude, variance explanation, and linear correlation for each model configuration. The best performing models were selected based on a balance between low prediction error and high generalization capability.

Overfitting Evaluation via Δ_{MSE}

To quantitatively assess the presence of overfitting, the percentage variation between the MSE on the training and validation sets was computed as:

$$\Delta_{MSE}(\%) = \frac{MSE_{validation} - MSE_{train}}{MSE_{train}} \cdot 100 \tag{12}$$

A large positive value of Δ_{MSE} indicates that the model performs significantly worse on unseen data, which is a typical sign of overfitting. Conversely, values close to zero suggest consistent generalization, while negative values may point to data variance or underfitting. This metric was used alongside validation performance monitoring to identify and discard models with poor generalization ability.

In addition, to further mitigate overfitting, the maximum number of validation failures was set to 2 by configuring the parameter `net.trainParam.max_fail = 2`. *This*

setting activates an early stopping mechanism that halts the training process if the validation performance does not improve for 2 consecutive iterations, thereby preventing the model from continuing to learn patterns specific to the training set.

2.3 Permutation feature analysis

To assess the relative influence of each input parameter on the predicted surface roughness, Permutation Feature Importance (PFI) was employed. PFI is a method that quantifies the importance of a feature by measuring the increase in prediction error when its values are randomly permuted, thereby disrupting its relationship with the target variable [74–76].

The baseline prediction error is computed on the unshuffled dataset as [74, 75]:

$$\mathcal{L}_{\text{base}} = \frac{1}{n}\sum_{i=1}^{n}\mathcal{L}\left(y_i, f(\mathrm{x}_i)\right) \tag{13}$$

where $f(\cdot)$ denotes the trained predictive model (in this study is ANN), $\mathrm{X} = [\mathrm{x}_1, \ldots, \mathrm{x}_n]^\top \in \mathbb{R}^{n\times p}$ is the original input matrix with *n* samples and *p* features, and $\mathrm{y} = [y_1, \ldots, y_n]^\top$ the vector of ground truth outputs. $\mathcal{L}(y, \hat{y})$ denote a generic loss function, in this study is adopted the MSE (Eq. 7).

To assess the importance of feature *j*, the values in column *j* of X are randomly permuted to generate a modified dataset $\mathrm{X}^{(j)}$, and the new predictions are given by $\hat{\mathrm{y}}^{(j)} = f(\mathrm{X}^{(j)})$.

The prediction error for this permuted dataset is [74, 75]:

$$\mathcal{L}^{(j)}_{\text{perm}} = \frac{1}{n}\sum_{i=1}^{n}\mathcal{L}\left(y_i, f(\mathrm{x}^{(j)}_i)\right) \tag{14}$$

The importance score of feature *j* is calculated as the increase in loss caused by the permutation of that feature, that is, the difference between the loss on the permuted data $\mathcal{L}^{(j)}_{\text{perm}}$ and the original baseline loss $\mathcal{L}_{\text{base}}$.

To obtain a robust estimate, the permutation is repeated *K* times and the average importance score is computed as [74, 75]:

$$\text{PFI}^{(j)} = \frac{1}{K}\sum_{k=1}^{K}\left(\mathcal{L}^{(j)}_{\text{perm},k} - \mathcal{L}_{\text{base}}\right) \tag{15}$$

In this study, the MSE was used as the loss function $\mathcal{L}$ to evaluate the prediction accuracy of the trained ANN for surface roughness. To compute PFI, each input feature was randomly permuted $K = 100$ times, and the average increase in MSE was recorded. The input matrix X included six variables: LPb, SSb, LPc, SSc, angle and height. The output vector y contained the corresponding experimental *Ra* values.For each feature *j*, the score $\text{PFI}^{(j)}$ quantifies how much the model's performance deteriorates when the feature's information is destroyed. High PFI values indicate strong influence on the prediction, while low values suggest minor relevance. This analysis allows ranking the process parameters based on their impact on *Ra*, supporting process understanding and optimization in LPBF.

2.4 AM parameters optimization for *Ra* minimization

During the optimization phase, the geometrical parameters Height and Angle were considered as fixed categorical inputs, representing distinct areas of the building volume. For each unique combination of these two parameters, a separate optimization problem was solved.

The remaining four variables (LP body, SS body, LP contour, SS contour) were treated as continuous decision variables, subject to lower and upper bounds derived from the original dataset. These variables were allowed to vary within the specified bounds in order to minimize the predicted surface roughness *Ra*, as estimated by the trained ANN model.

From a practical standpoint, this was achieved by filtering and grouping the dataset according to the geometric parameters (Height and Angle). Each group represents a specific combination of these two parameters, corresponding to a distinct region of the build volume. Once the data were structured in this way, the optimization was performed separately for each group, by varying the four process parameters (LPb, SSb, LPc, SSc) within their respective bounds to minimize the predicted *Ra*.

The MATLAB `fmincon` [77] solver was used to minimize the predicted *Ra* from the trained ANN model by optimizing the selected process parameters within predefined bounds. The optimization problem is formulated as [77, 78]:

$$\min_{x} f(x) \quad \text{subject to} \quad \text{lb} \le x \le \text{ub} \tag{16}$$

where *f*(*x*) is the objective function corresponding to the *Ra* value predicted by the neural network, $x \in \mathbb{R}^n$ is the vector of decision variables (LPb, SS_{body}, LPc, SSc), and lb, ub represent the lower and upper bounds for each variable, respectively. The bounds were defined based on the minimum and maximum experimentally tested values to ensure a physically meaningful search domain.

The optimization was performed using the Sequential Quadratic Programming (SQP) algorithm implemented in

the `fmincon` solver, which iteratively refines a quadratic approximation of the objective function and updates the solution until convergence to a local minimum is achieved [78].

For each fixed pair (Height, Angle), the solver searched the feasible space of the continuous inputs to identify the combination that yielded the lowest predicted *Ra* value, within the specified constraints. The optimization search is therefore carried out individually for each specific combination of height and angle. This makes it possible to identify distinct process parameter combinations for different regions of the build space, which may lead to different surface quality outcomes depending on the local geometric conditions. In this way, the method provides the basis for a spatially adaptive process strategy, where the optimal parameters can vary according to the position within the part.

3 Results and discussion

3.1 Neural network

Table 4 presents the performance comparison of various ANN training algorithms based on standard regression metrics, including MSE, RMSE, MAE, R^2, and the percentage variation of MSE on the validation set.

Among all the tested algorithms, Bayesian Regularization yielded the most promising results, achieving the lowest MSE (4.6338), RMSE (2.1526), and MAE (1.6457), along with the highest R^2 value (0.7726), indicating the best predictive accuracy. Additionally, it exhibited a negative $\Delta_{\mathrm{MSE}}(\%)$ on validation (-6.27%), which may suggest a slight underfitting, as the model performs marginally better on the validation data than on the training set. In addition to Bayesian Regularization, the Levenberg–Marquardt algorithm also demonstrated strong predictive performance in estimating surface roughness *Ra*. These findings are in line with those reported by Jakšić et al. [79], where Bayesian Regularization, Levenberg–Marquardt, and Scaled Conjugate Gradient were identified as the most effective training algorithms.

Based on these results, Bayesian Regularization was selected as the optimization algorithm for further investigation. Subsequently, the effect of varying the number of hidden layers and the number of neurons per layer was studied, while keeping the training algorithm fixed. The results of performance metrics of several ANN architectures are reported in Table 5.

Among all configurations tested, the architecture comprising a single hidden layer with 30 neurons yielded the most optimal results, with the lowest MSE (3.187), RMSE (1.7852), MAE (1.4254) and the highest determination coefficient R^2 (0.8436). This configuration indicates a well generalized model with minimized prediction error. Increasing the number of neurons to 40, while still maintaining a single hidden layer, resulted in a slight degradation in performance (e.g., increased MSE and RMSE). Similarly, the introduction of a second or third hidden layer (with 10 or 20 neurons) led to architectures with comparable but generally inferior performance metrics. Although some of these multilayer configurations approached the performance of the single layer, 30 neurons model, they consistently exhibited higher MSE, RMSE, and MAE, along with a reduction in R^2. In addition, a noticeable increase in Δ_{MSE} was observed in deeper architectures, further supporting the hypothesis of overfitting risk when increasing model complexity beyond the optimal configuration.

To investigate the impact of the activation function, an additional test was performed on the optimal architecture (single hidden layer with 30 neurons) using the logarithmic sigmoid function (logsig). The results of Table 6 demonstrated a marked deterioration in performance: MSE increased to 6.7489, RMSE increased to 2.5979, MAE

Table 4 Regression metrics, training algorithm comparison

Algorithm	MSE	RMSE	MAE	R^2	$\Delta_{\mathrm{MSE}}(\%)$	r
Levenberg-Marquardt	4.8896	2.2112	1.6926	0.7601	14.1428	0.87
Bayesian Regularization	4.6338	2.1526	1.6457	0.7726	-6.2681	0.88
BFGS Quasi-Newton	9.7636	3.1247	2.4651	0.5209	19.2482	0.72
Resilient Backpropagation	5.1513	2.2696	1.7255	0.7472	-1.928	0.86
Scaled Conjugate Gradient	11.0778	3.3283	2.7576	0.4564	6.454	0.68
Conjugate Gradient with Powell/Beale Restarts	7.5402	2.7459	2.1423	0.63	-4.7037	0.8
Fletcher-Powell Conjugate Gradient	9.2118	3.0351	2.3299	0.548	10.8467	0.74
Polak-Ribiére Conjugate Gradient	11.1785	3.3434	2.6294	0.4515	1.3989	0.67
One Step Secant	12.5465	3.5421	2.7957	0.3843	-16.6291	0.64
Variable Learning Rate Gradient Descent	8.6409	2.9395	2.3547	0.576	13.386	0.76
Gradient Descent with Momentum	10.0144	3.1645	2.4577	0.5086	38.5437	0.72
Gradient Descent	10.999	3.3165	2.6588	0.4603	26.827	0.68

Table 5 Regression metrics, number of neurons and hidden layer comparison with fixed Bayesian Regularization algorithm

	Hidden L.1	Hidden L.2	Hidden L.3	MSE	RMSE	MAE	R^2	$\Delta_{MSE}(\%)$	r
Number of neurons	10	0	0	4.6338	2.1526	1.6457	0.7726	-6.2681	0.88
	20	0	0	6.5217	2.5538	1.9443	0.68	26.7061	0.82
	30	0	0	3.187	1.7852	1.4254	0.8436	-1.6882	0.92
	40	0	0	3.2287	1.7969	1.4147	0.8416	15.4952	0.92
	10	10	0	3.6698	1.9157	1.4813	0.8199	59.0568	0.91
	20	10	0	5.3295	2.3086	1.742	0.7385	-28.6441	0.86
	30	10	0	3.6673	1.915	1.4629	0.82	30.1469	0.91
	30	20	0	3.2271	1.7964	1.3626	0.8416	42.8594	0.92
	30	10	10	3.944	1.986	1.5637	0.8065	20.9209	0.90
	30	20	10	4.0835	2.0208	1.5285	0.7996	28.9391	0.90

Table 6 Regression metrics, activation function comparison

Act. Fun.	MSE	RMSE	MAE	R^2	$\Delta_{MSE}(\%)$	r
tansig	3.187	1.7852	1.4254	0.8436	-1.6882	0.92
logsig	6.7489	2.5979	1.9558	0.6688	1.2216	0.82

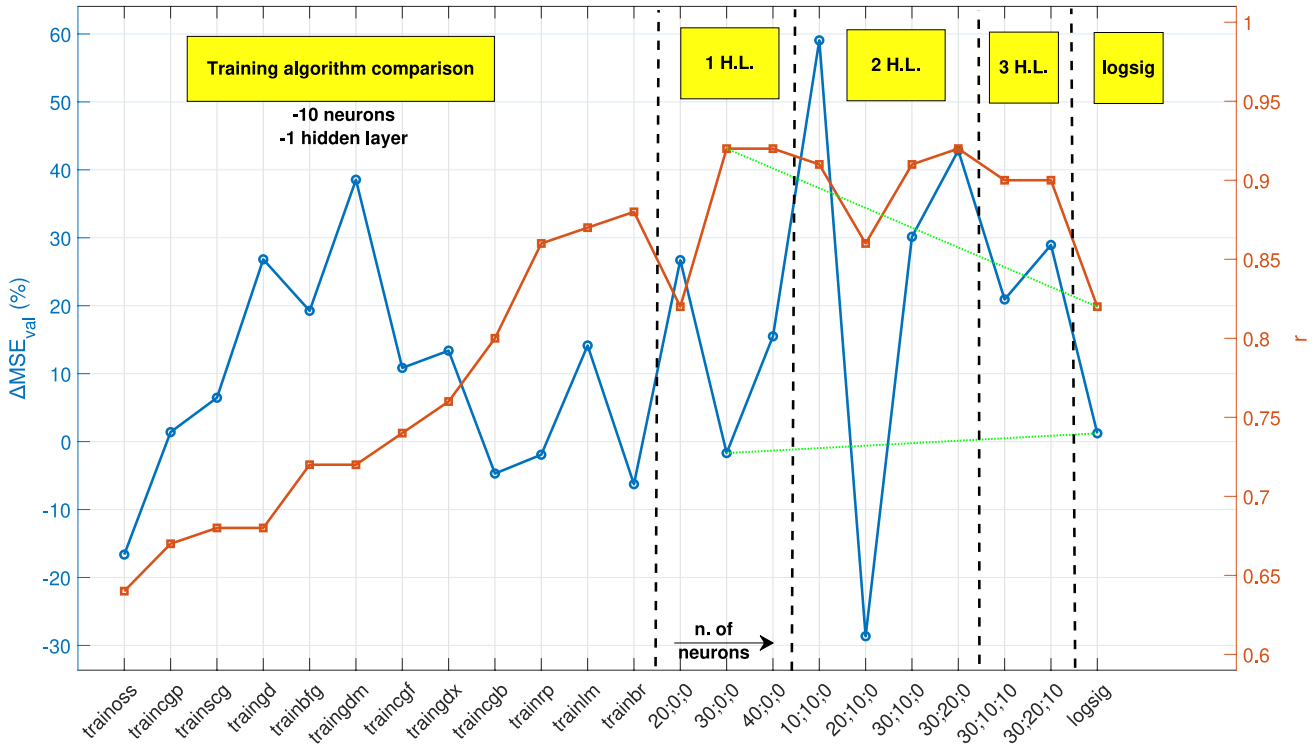

Fig. 7 Graphical comparison of neural network performance across multiple configurations

reached 1.9558, and R^2 decreased to 0.6688. This comparison highlights the importance of the choice of activation function and confirms that, for the present dataset and regression task, tansig is more effective than logsig.

Figure 7 presents a comprehensive comparison of network configurations in terms of the Pearson correlation coefficient (*r*, right y-axis) and ΔMSE_{val} (left y-axis). The x-axis is divided into distinct sections, each corresponding to a specific aspect of the neural network architecture or training strategy. In the first section, the impact of the training algorithm is assessed. Here, the architecture is characterized by a single hidden layer composed of 10 neurons. As shown, performance varies significantly depending on the algorithm employed. Notably, the Bayesian Regularization algorithm (`trainbr`) yielded one of the lowest ΔMSE_{val} values (-6.27%) and one of the highest *R* values (0.88).

Table 7 Main parameters of the ANN used for surface roughness *Ra* prediction

Parameter	Value
Number of hidden layers	1
Neurons in the hidden layer	30
Activation function (hidden layer)	Hyperbolic tangent sigmoid (tansig)
Activation function (output layer)	Linear (purelin)
Maximum number of training epochs	1000
Data set partition	70% training 15% validation 15% test
Loss function	Mean Squared Error (MSE)
Training algorithm	Bayesian Regularization
Maximum number of validation failures	2

The following three sections explore the influence of the network architecture using Bayesian Regularization as the fixed training algorithm. In the second section, the number of neurons in the first hidden layer is varied from 20 to 40. The configuration with 30 neurons (labelled as `30_0_0`) achieved the best overall performance, with the lowest ΔMSE_{val} (-1.69%) and the highest R (0.92). In the third and fourth sections, the number of hidden layers is increased to two and three, respectively. Various combinations of neurons were tested, and while some of the multilayer architectures produced acceptable results, none surpassed the performance of the single-layer configuration with 30 neurons. In addition, several configurations exhibited high positive ΔMSE_{val} values, indicative of potential overfitting and reduced generalization capability. The final section investigates the effect of the transfer function. Specifically, the `logsig` function was applied to the previously optimal configuration (`30_0_0`), replacing the standard `tansig`. To facilitate visual comparison, the corresponding data points for `logsig` and `tansig` are connected by a green dashed line.

Overall, the results show that:

- The choice of training algorithm substantially influences the generalization ability, with Bayesian Regularization offering the best balance between low validation error and high correlation.
- Increasing the number of neurons in a single hidden layer improves model accuracy up to a certain point, beyond which performance plateaus or deteriorates;

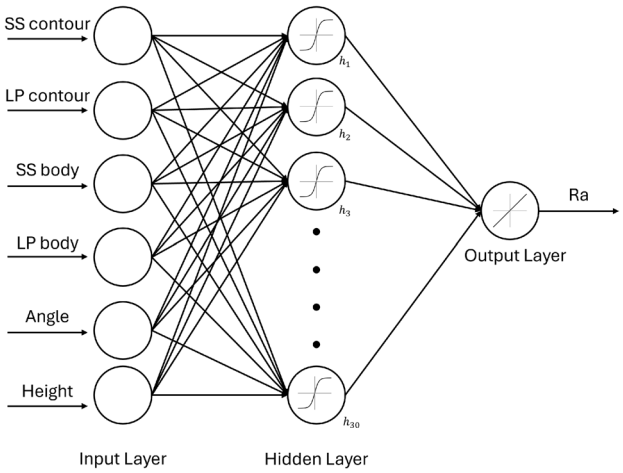

Fig. 8 Artificial Neural Network architecture

- Adding more hidden layers does not necessarily lead to better performance and may increase the risk of overfitting;
- The `tansig` transfer function outperforms `logsig` in this specific application, confirming its suitability for the neural network configuration adopted.

The parameters ultimately selected for the ANN, based on the performance evaluations described above, are reported in Table 7. A schematic illustration of the ANN architecture is presented in Fig. 8.

The regression plots for the training, validation, and test sets are shown in Fig. 9. The predicted outputs are plotted against the actual target values. In an ideal case, all data points would lie along the 45°line, indicating a perfect prediction. The quality of the regression was assessed using the Pearson Correlation Coefficient r for each subset. The r values obtained are 0.923 for the training set, 0.919 for the validation set, and 0.896 for the test set. These values are very close to each other, indicating that the network is able to generalize well to unseen data without signs of overfitting. The overall correlation coefficient, calculated for the entire dataset, is $r = 0.918$, further confirming the robustness and stability of the trained model in all data partitions.

Figure 10 illustrates the MSE performance of the neural network during training. The network achieved its best validation performance at epoch 35, with an MSE of 0.026867. The convergence trend indicates consistent error reduction across training, validation, and test sets, with no significant overfitting. For the test dataset, the MSE slightly increases from epoch 32 (MSE=0.0310) to epoch 35 (MSE=0.0332), corresponding to an approximate rise of 7%, which may indicate the onset of mild overfitting;

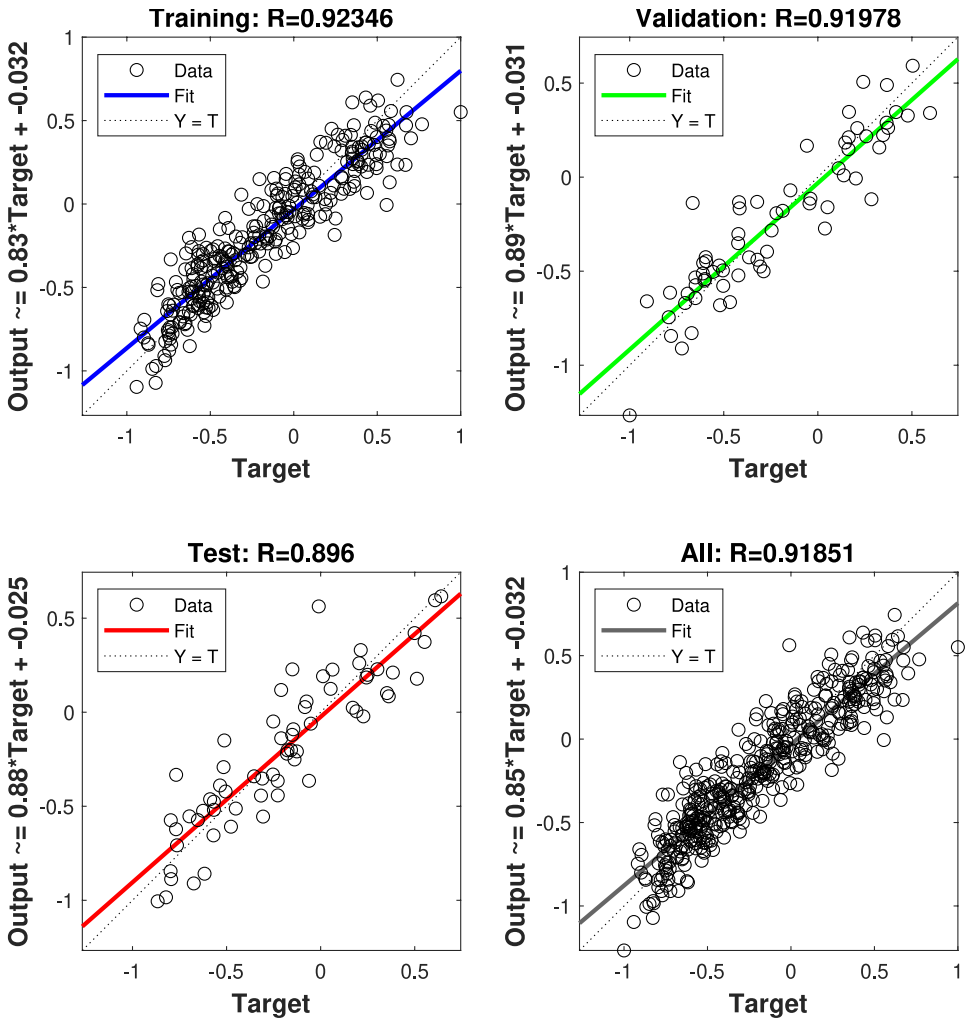

Fig. 9 Regression plots showing the correlation between predicted and target Ra values for training, validation, test, and overall datasets

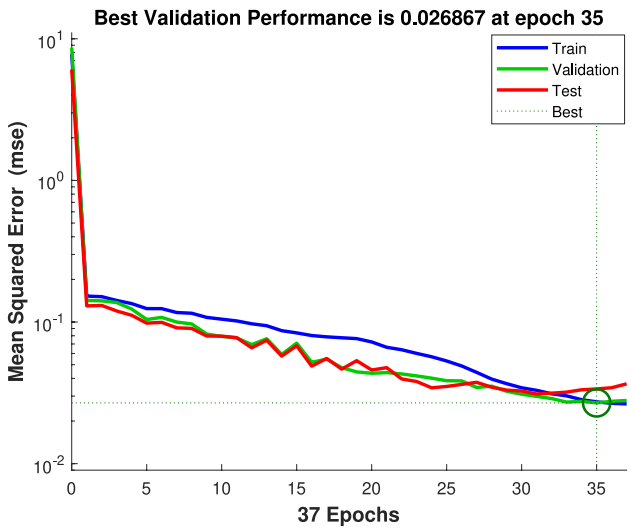

Fig. 10 Mean Squared Error evolution for training, validation, and test datasets

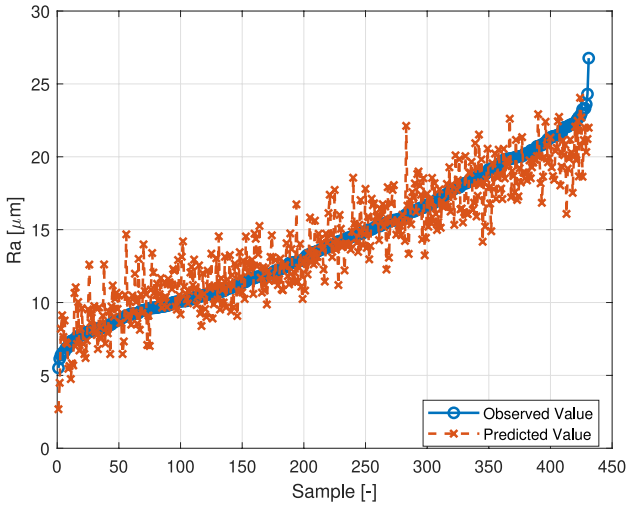

Fig. 11 Comparison between the predicted and observed R_a values

however, this variation remains within an acceptable range for good generalization.

This suggests a well-generalized model capable of maintaining predictive accuracy on unseen data.

Figure 11 shows the comparison between the observed and predicted surface roughness values *Ra* in all samples. The blue circles represent the observed values, while the red crosses indicate the predicted values obtained from the model. The close alignment between the two trends demonstrates good predictive performance.

3.2 Permutation feature importance

Figure 12 shows the computed PFI for each input variable in predicting surface roughness, as measured by the average increase in MSE after permutation.

Among all process parameters, the contour laser power and scanning speed exhibited the highest influence on surface roughness prediction, with respectively ΔMSE approaching $42\mu m^2$ and $23\mu m^2$. This highlights the key role of contour processing in determining the final surface finish, especially at the external boundaries of the part.

Other significant contributors include the scanning speed in the body region and the angle, with ΔMSE values around $10\mu m^2$ and $11\mu m^2$, respectively. The laser power in the body region and the build angle show moderate influence, while build height was found to have the lowest impact on the predicted roughness.

The body laser power and height were found to have the lowest impact on the predicted roughness with respectively ΔMSE $5\mu m^2$and $4\mu m^2$

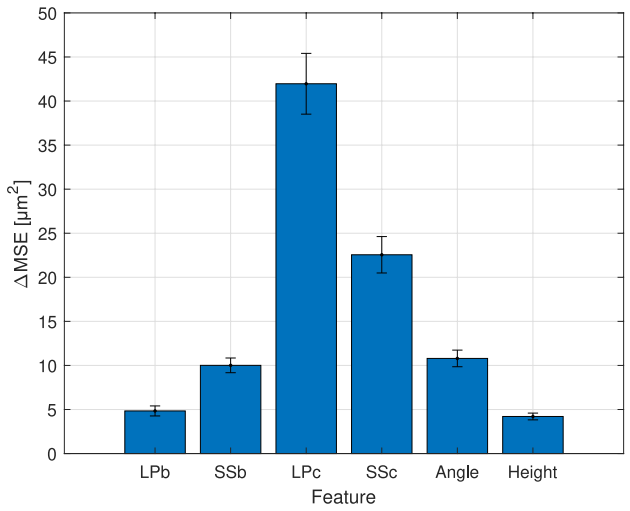

Fig. 12 Permutation Feature Importance based on the average MSE increase

These results are consistent with the physical understanding that contour parameters govern the quality of external surfaces more directly than internal process variables.

The influence of process parameters on surface roughness in LPBF arises from the thermal and fluid dynamic behavior of the melt pool, especially in the interaction between contour and body regions. As demonstrated by Zhang and Yuan [80], the SSc plays a dominant role in defining the final surface quality. Low scanning speeds increase the energy input, producing deeper and more stable melt pools that promote smooth, continuous scan tracks with minimal dross formation. In contrast, higher SSc leads to insufficient energy input, resulting in incomplete melting, instability at the melt pool edges, and the accumulation of partially fused particles, all of which contribute to increased roughness. Similarly, excessive LPc can amplify melt pool instability, especially when combined with high scanning speeds, further degrading the surface finish [80].

In addition to the contour parameters, the body region also can affect surface roughness through melt pool overlap. When the energy input in the body region is low, the contour controls the surface quality. However, at higher body energy densities, the melt pool generated during body scanning may overlap and partially remelt the previously solidified contour tracks. This overlap disrupts the stability and continuity of the contour, increasing surface roughness. The physical origin of this behavior lies in the lateral expansion of the body melt pool, which, if not properly confined, invades the contour region and alters the morphology of the outer surface [80]. These results underline the need for carefully balancing energy input across both scan regions to maintain surface integrity.

Although build height was not among the most influential factors in the sensitivity analysis, its contribution to surface roughness remains relevant. As the build progresses, the part moves further away from the base plate, and the efficiency of heat extraction through the build platform decreases. In the early stages of the process, lower layers benefit from stronger thermal sinking and more stable melt dynamics. However, in higher sections of the part, the reduced thermal dissipation can alter the cooling rate and disrupt melt pool stability, which may lead to the formation of surface inconsistencies such as balling or waviness. Experimental studies have confirmed that the thermal environment changes along the vertical axis of the build. For example, Ulbricht et al. [34] observed that microstructural features in LPBF specimens tend to be more homogeneous near the base, where thermal conduction is more favorable. In contrast, upper sections showed signs of altered solidification behavior due to less effective heat removal. Furthermore, research by Serrano-Muñoz et

Table 8 Optimal process parameters and corresponding predicted surface roughness values obtained from the neural network

Angle	Height	LPb	SSb	LPc	SSc	*Ra*
[°]	[mm]	[W]	[mm/s]	[W]	[mm/s]	[μm]
0	15	220	1000	207	431	6.26
	35	220	1000	214	456	7.30
	55	220	1000	220	480	6.94
90	15	220	1000	203	416	4.61
	35	220	1000	211	444	6.55
	55	220	1000	218	470	6.64
180	15	280	800	189	389	3.46
	35	280	800	194	407	5.10
	55	280	800	200	428	4.77

Table 9 Lowest surface roughness values and corresponding process parameters identified from physical measurements

Angle	Height	LPb	SSb	LPc	SSc	*Ra*
[°]	[mm]	[W]	[mm/s]	[W]	[mm/s]	[μm]
0	15	220	800	180	300	7.52
	35	280	1000	220	400	7.45
	55	220	800	180	300	8.15
90	15	280	1000	180	300	6.39
	35	220	800	180	300	7.97
	55	220	800	180	300	8.08
180	15	220	800	180	300	5.51
	35	220	800	180	300	6.14
	55	220	800	220	400	6.63

al. [35] indicated that residual stress tends to increase with height, which indirectly reflects variations in the thermal gradient and melt pool behavior. These findings support the idea that roughness may be more prone to variation at elevated heights, especially in the absence of adaptive process control.

The angular orientation in the XY plane relative to the recoater blade movement has been found to influence surface roughness. This effect can be attributed to the interaction between the recoater and the local powder bed environment. Depending on the surface orientation, the distribution of powder particles during recoating may vary slightly due to differences in how the blade interacts with edges and local geometry.

3.3 AM parameters optimization for *Ra* minimization

Tables 8 and 9 report the optimal process parameters and the corresponding surface roughness (R_a) values obtained for each combination of angle and height. The first table presents the values predicted by the neural network, while the second table reports the lowest R_a values measured experimentally, allowing a direct comparison between predicted and physical results.

By comparing the results in Table 8 with those in Table 9, it is possible to explore the effect of non-experimentally tested combinations of process parameters on the resulting surface roughness. A key observation is that, for each combination of build angle and height, the ANN was able to identify a set of process parameters that lead to lower *Ra* values compared to those obtained experimentally. In particular, the combination of SSb = 1000 mm/s and LPb = 220 W (which was not tested during the experimental campaign) appears to be the most effective configuration for the body scan parameters at angles of 0°and 90°at all height levels. Across all samples, the parameters associated with the contour region exhibit greater variability than those of the body region. Moreover, the network predicted a minimum *Ra* value of 3.46 µm at Height = 15 mm and Angle = 180°, compared to the corresponding experimental value of 5.51 µm obtained under the same geometric conditions. On average, the optimization led to a reduction in surface roughness of approximately 19.4% across all evaluated geometric positions, demonstrating the potential of the proposed ANN based framework to enhance surface quality.

Moreover, the ANN demonstrated spatial awareness by adapting parameter settings based on geometric variations, such as build height and angular orientation. For instance, it adjusted the contour parameters at higher z-levels to compensate for decreased heat dissipation, and tailored scan conditions based on the part's orientation relative to the recoater blade–an approach that was not implemented in the experimental design. These findings open the possibility of

implementing a spatially adaptive process parameter strategy, where the laser power and scanning speed are varied locally based on the part's geometric position, specifically, the build angle and height. Since the optimal Ra values predicted by the ANN differ across angle–height combinations, adopting a uniform set of parameters throughout the build may not be sufficient to ensure globally minimized roughness. Instead, tailoring the body and contour parameters for each geometric zone can allow for better control over melt pool behavior, heat dissipation, and powder consolidation dynamics. This localized tuning approach has the potential to enhance surface quality systematically, compensating for the thermal and morphological variations inherent to different orientations and vertical locations. From a practical perspective, this concept could be implemented by segmenting the geometry of the part to be printed according to its height and orientation. Each segment would correspond to a specific geometric zone, allowing the assignment of different process parameter values depending on the location. This strategy could be applied during the slicing stage, enabling local tuning of laser power and scanning speed throughout the build and effectively adapting the process to the specific geometry of the component.

One of the primary reasons for the improved surface roughness achieved by the ANN optimized parameters lies in its ability to tune the energy input involved in the generation of the melt pool. If the energy input is too high, it can cause overheating of the powder bed, leading to defects such as balling, keyholing, excessive spatter, and melt pool instability. These phenomena result in rough, irregular surfaces due to the uncontrolled melting pool solidification and to the accumulation of partially fused particles. Conversely, if the energy input is too low, the powder may not fully melt, leading to incomplete fusion, porosity, and weak bonding between layers, which also contribute to high surface roughness. The ANN is able to predict parameter combinations that balance laser power and scanning speed to stay within the optimal energy window, avoiding both thermal extremes. A notable example from the optimized results is the prediction of LPb = 220 W and SSb = 1000 mm/s, a combination not tested experimentally but shown by the ANN to consistently minimize roughness. This pairing achieves a moderate energy density that prevents overheating while ensuring sufficient melting, leading to more uniform melt pools, smoother track consolidation, thus improved surface morphology. By avoiding excessive or insufficient energy input, the ANN ensures thermal stability of the melt pool, promotes uniform layer solidification, and enhances the final surface finish. Importantly, the ANN was trained using Bayesian Regularization, a technique that effectively mitigates overfitting by penalizing overly complex models. This ensured that the network generalized well to unseen parameter combinations, as evidenced by consistent predictive performance across training, validation, and test datasets ($R^2 = 0.8436$, $r = 0.918$). As a result, the ANN not only replicated known trends but also identified physically meaningful process settings that surpassed the best outcomes achieved through experimental trials alone.

While this study focuses exclusively on surface roughness as the target output, it is acknowledged that other thermomechanical properties (e.g. porosity, hardness,thermal conductivity) are also influenced by the process parameters and may be impacted by the optimization outputs. In a separate investigation [38], the effects of process parameters on these additional properties were systematically evaluated. That study identified an optimal processing window for improved thermomechanical performance at LPb = 250 W and SSb = 800 mm/s.Building on those findings, the search for minimum *Ra* was refined by adjusting the lower and upper bounds of the optimization space. Specifically, the bounds for LPb and SSb were constrained to the following intervals to reflect the process window favorable for thermomechanical properties:

Table 10 Optimized process parameters for minimizing *Ra*, with refined bounds on LPb and SSb

		ANN					Physical Measurements				
Angle	Height	LPb	SSb	LPc	SSc	Ra	LPb	SSb	LPc	SSc	Ra
[°]	[mm]	[W]	[mm/s]	[W]	[mm/s]	[μm]	[W]	[mm/s]	[W]	[mm/s]	[μm]
0	15	260	820	204	457	11.56	250	800	220	500	11.77
0	35	250	800	220	500	11.77	250	800	220	500	11.77
0	55	260	820	210	480	13.40	250	800	220	500	14.53
90	15	260	820	204	451	8.39	250	800	180	400	10.56
90	35	250	800	220	500	10.66	250	800	220	500	10.66
90	55	250	800	220	500	11.30	250	800	220	500	11.30
180	15	260	780	190	425	4.42	250	800	220	500	6.90
180	35	260	780	195	444	5.93	250	800	180	400	7.72
180	55	260	780	203	468	5.62	250	800	220	500	8.17

$$\text{LPb} \in [240, 260]\ \text{W}, \qquad \text{SSb} \in [780, 820]\ \text{mm/s}$$

The updated parameter combinations resulting from the refined search bounds are summarized in Table 10, along with the optimal results obtained by fixing LPb and SSb (250W and 800mm/s) and optimizing the other parameters. As a result of this refined optimization, a minimum predicted surface roughness of $Ra = 4.42\ \mu$m was achieved for a sample built at an angle of 180° and a height of 15 mm. Overall, this corresponds to a reduction of 18.65% compared to the experimentally measured *Ra* obtained with the standard parameters (LPb = 250 W, SSb = 800 mm/s) at the same geometric conditions.

The proposed ANN based framework is fully generalizable and can be applied to different LPBF materials, including conventional alloys and novel metal matrix composites, provided that appropriate experimental datasets are available. Moreover, the input space can be expanded to include additional process parameters such as hatch spacing, layer thickness, or the position on the build plate, allowing for a more comprehensive optimization of the process property relationship.

Although the developed ANN model achieved robust predictive performance, it is important to acknowledge that, in general, the reliability and generalization capability of neural networks are known to benefit significantly from the availability of large and diverse training datasets. Prior studies have demonstrated that increasing the amount of training data can systematically improve prediction accuracy and model stability [81].

4 Conclusion

The aim of this study was to develop a predictive model based on an artificial neural network capable of estimating the effects of key process parameters on surface roughness in LPBF. Furthermore, the model was used to determine the optimal combination of input parameters that minimizes surface roughness for different regions of the build volume–defined by variations in part orientation and height.

Through a sequential model adjustment, a feedforward ANN with a single hidden layer of 30 neurons, hyperbolic tangent activation, and Bayesian Regularization was developed to predict surface roughness (*Ra*) based on four process parameters (LPb, LPc, SSb, SSc) and two geometrical factors (Angle and Height). The network achieved satisfactory predictive performance (MSE = 3.187, MAE = 1.4254, R^2 = 0.8436, RMSE = 1.7852, Δ_{MSE} = –1.6882%), demonstrating its ability to generalize beyond the experimental dataset. Permutation feature importance revealed that the laser power in the contour region had the greatest influence on roughness. The model was then applied to identify optimal process parameters for each geometric condition, predicting lower *Ra* values than those experimentally measured. Notably, the combination SSb = 1000 mm/s and LPb = 220 W, not included in the physical tests, showed consistently superior results at 0°and 90°build angles. These findings demonstrate the ANN's capability to adapt process parameters to local geometrical variations, paving the way for spatially adaptive strategies that could enhance surface quality by compensating for thermal and morphological effects throughout the build volume.

Although the ANN does not explicitly model physical phenomena, the learned relationships between inputs and predicted surface roughness align with established physical principles. In particular, the high importance attributed to contour laser power and scanning speed in the PFI analysis reflects their well known influence on melt pool stability and surface quality.

Overall, this work highlights the potential of ANN in data driven process optimization for AM, offering a powerful alternative to empirical or trial and error methods. The model developed in this study could serve as a decision support tool to guide parameter selection and improve the quality and efficiency of LPBF processes.

The novelty of this work lies in the integration of geometric factors (build angle and height) into an ANN-based framework, enabling localized optimization of process parameters for surface roughness reduction. Future work will focus on validating the predicted optimal parameters experimentally and implementing spatially adaptive process strategies during slicing to enhance surface quality and industrial applicability. In addition, future developments may incorporate more sophisticated optimization frameworks to systematically refine the model architecture, enhance hyperparameter selection, and ultimately improve predictive performance.

Appendix A Dataset used for neural network training

The complete dataset used for training the neural network model is presented in Table 11. This table includes all input and output variables:

- LPc: Contour Laser Power;
- SSc: Contour Scanning Speed;
- LPb: Body Laser Power;
- SSb: Body Scanning Speed;
- Angle: Part orientation angle;
- Height: Part height;
- Ra: Surface roughness.

Table 11 Complete dataset used for training the neural network model, reporting all input parameter combinations and the corresponding measured surface roughness values (R_a)

Angle [°]	Height [mm]		LPc= 140W; SSc= 300mm/s Ra [μm]	LPc= 180W; SSc= 300mm/s Ra [μm]	LPc= 180W; SSc= 400mm/s Ra [μm]	LPc= 180W; SSc= 500mm/s Ra [μm]	LPc= 220W; SSc= 400mm/s Ra [μm]	LPc= 220W; SSc= 500mm/s Ra [μm]		LPc= 140W; SSc= 300mm/s Ra [μm]	LPc= 180W; SSc= 300mm/s Ra [μm]	LPc= 180W; SSc= 400mm/s Ra [μm]	LPc= 180W; SSc= 500mm/s Ra [μm]	LPc= 220W; SSc= 400mm/s Ra [μm]	LPc= 220W; SSc= 500mm/s Ra [μm]
0	15	LPb= 220W; SSb= 800mm/s	26.77	7.52	21.40	19.61	12.69	16.71	LPb= 250W; SSb= 900mm/s	22.011	15.13	11.91	15.06	15.25	11.27
0	35		23.60	10.37	21.84	17.60	10.84	20.46		20.04	22.25	19.17	16.27	18.68	11.59
0	55		21.58	8.15	22.03	17.05	9.28	20.21		19.25	18.71	16.83	16.85	20.02	12.14
90	15		21.42	6.49	17.95	18.29	12.89	15.77		23.25	14.43	10.55	14.48	12.38	8.25
90	35		18.73	7.97	20.02	20.22	13.47	19.15		24.30	20.27	15.57	18.20	15.72	10.70
90	55		18.32	8.08	21.37	17.75	15.00	17.44		20.92	19.78	14.73	16.49	19.34	12.35
180	15		10.70	5.51	8.50	10.58	7.37	8.73		13.94	10.04	8.97	11.64	10.09	8.38
180	35		12.80	6.14	11.12	13.38	8.18	7.98		16.05	15.00	9.79	13.80	12.38	10.90
180	55		15.79	6.86	9.07	12.84	6.63	8.31		18.55	16.77	9.49	14.82	14.27	11.88
0	15	LPb= 250W; SSb= 800mm/s	22.95	15.68	15.86	19.54	16.34	11.77	LPb= 280W; SSb= 900mm/s	21.51	13.91	14.62	18.50	9.44	9.83
0	35		21.01	14.88	22.74	19.43	21.62	11.77		22.74	17.69	20.80	16.39	13.43	12.29
0	55		19.85	17.87	20.43	21.22	21.24	14.53		22.60	16.38	16.70	20.48	11.69	16.54
90	15		20.28	11.61	10.56	22.05	14.24	11.40		17.83	10.11	8.85	13.71	7.85	9.23
90	35		18.94	18.80	13.46	19.83	19.96	10.66		20.73	17.82	13.63	15.24	9.06	10.22
90	55		17.90	18.12	15.84	18.79	20.88	11.30		22.33	19.71	15.20	15.63	12.42	9.81
180	15		13.71	6.93	7.13	10.77	7.79	6.90		15.25	9.01	10.61	11.96	8.46	10.63
180	35		16.71	9.21	7.72	12.99	9.63	8.03		16.52	12.88	11.92	15.67	11.18	9.63
180	55		15.52	11.87	8.24	15.48	10.36	8.17		16.24	12.75	11.84	15.58	10.12	10.99
0	15	LPb= 280W; SSb= 800mm/s	23.32	14.54	9.47	22.07	15.34	10.01	LPb= 250W; SSb= 1000mm/s	20.00	10.37	13.27	13.59	8.42	10.72
0	35		21.50	16.03	16.17	23.29	18.19	14.35		21.41	11.05	13.53	15.74	10.80	9.24
0	55		19.85	19.87	19.89	22.18	21.07	12.87		20.20	10.06	13.93	14.71	9.50	11.01
90	15		18.87	10.11	7.68	15.33	11.40	8.64		13.27	6.6	9.21	11.54	7.95	9.58
90	35		20.56	18.72	9.63	16.48	17.52	9.90		15.65	9.64	10.46	14.42	8.90	11.07
90	55		20.11	22.14	12.46	19.34	19.24	12.54		16.81	9.23	11.13	16.50	10.55	10.43
180	15		13.08	8.21	7.35	10.02	8.30	7.96		15.41	7.66	9.73	14.67	7.70	9.65
180	35		16.09	9.67	7.90	13.21	10.65	8.12		13.91	9.77	10.23	13.75	9.46	9.66
180	55		18.15	14.02	9.58	14.33	10.57	9.52		19.99	10.25	11.65	14.60	10.38	12.22
0	15	LPb= 220W; SSb= 900mm/s	20.74	14.15	11.80	15.19	11.43	9.71	LPb= 280W; SSb= 1000mm/s	22.48	10.16	18.74	17.06	9.25	11.83
0	35		19.97	15.60	11.98	17.34	16.26	9.72		21.45	12.19	14.59	17.31	7.45	12.26
0	55		18.55	19.90	14.21	17.61	17.89	11.86		22.22	12.80	14.23	14.72	8.64	10.95
90	15		20.46	10.10	8.44	10.58	10.39	9.38		13.96	6.39	13.44	14.47	8.26	11.35
90	35		21.32	19.16	12.73	14.99	17.37	11.65		19.18	9.22	15.99	15.65	9.73	12.77
90	55		20.71	20.80	16.23	15.42	18.37	14.17		18.41	10.78	16.69	17.02	10.08	12.73
180	15		12.71	9.10	7.41	9.75	8.73	8.33		22.25	8.86	12.04	13.56	10.45	10.23
180	35		17.24	11.77	8.79	13.27	11.72	9.12		19.84	10.11	17.05	18.16	10.46	12.18
180	55		18.48	14.80	9.92	14.95	13.82	10.05		19.89	13.72	17.05	15.03	11.30	10.99

Fig. 13 PNRR logo

Author Contributions **Delio Lusicini:** Conceptualization; Data curation; Investigation; Methodology; Writing - original draft; Materials Definition, Process parameters. **Matteo Crachi:** Conceptualization; Data curation; Funding acquisition; Investigation; Methodology; Writing - original draft; Materials Definition, Process parameters. **Raffaella Sesana:** Conceptualization; Supervision; Writing - review & editing. **Cristiana Delprete:** Conceptualization; Supervision; Writing - review & editing. **Marco Pizzarelli:** Writing - review & editing. **Nicola Sicignano:** Materials Definition, Process parameters. **Domenico Borrelli:** Materials Definition, Process parameters. **Antonio Caraviello:** Funding Acquisition, Supervision.

Funding The authors gratefully thank ASI (Italian Space Agency) for financial support of PhD research activity which lead to the present results.
This publication is part of the project PNRR-NGEU which has received funding from the MUR–DM 118/2023 (Fig. 13).

Data Availability The datasets generated during and/or analysed during the current study are available from the corresponding author on reasonable request.

Declarations

Competing interests The authors declare that they have no known competing financial interests or personal relationships that could have appeared to influence the work reported in this paper.

References

1. Lee YS, Zhang W (2015) Mesoscopic simulation of heat transfer and fluid flow in laser powder bed additive manufacturing. Int J Heat Mass Transf 88:709–720
2. Mumtaz K, Hopkinson N (2009) Top surface and side roughness of inconel 625 parts processed using selective laser melting. Rapid Prototyp J 15(2):96–103. https://doi.org/10.1108/13552540910943397
3. Qiu C, Panwisawas C, Ward M, Basoalto HC, Brooks JW, Attallah MM (2015) On the role of melt flow into the surface structure and porosity development during selective laser melting. Acta Materialia 96:72–79. https://doi.org/10.1016/j.actamat.2015.06.004
4. Guo M, Gu D, Xia L, Zhang H, Zhang J, Yang J, Wang R (2019) Selective laser melting additive manufacturing of pure tungsten: Role of volumetric energy density on densification microstructure and mechanical properties. Int J Refract Met Hard Mater 84:105025. https://doi.org/10.1016/j.ijrmhm.2019.105025
5. Balbaa M, Mekhiel S, Elbestawi M, McIsaac J (2020) On selective laser melting of inconel 718: Densification surface roughness and residual stresses. Mater Des 193:108818. https://doi.org/10.1016/j.matdes.2020.108818
6. Chowdhury S, Yadaiah N, Prakash C, Ramakrishna S, Dixit S, Gupta LR, Buddhi D (2022) Laser powder bed fusion: a state-of-the-art review of the technology materials properties & defects and numerical modelling. J Mater Res Technol 20:2109–2172. https://doi.org/10.1016/j.jmrt.2022.07.121
7. Liu J, Ye J, Silva Izquierdo D, Vinel A, Shamsaei N, Shao S (2023) A review of machine learning techniques for process and performance optimization in laser beam powder bed fusion additive manufacturing. J Intell Manuf 34(8):3249–3275. https://doi.org/10.1007/s10845-022-02012-0
8. Cui C, Cao G, Li X, Gao Z, Liu J, Liu Z (2023) A strategy combining machine learning and physical metallurgical principles to predict mechanical properties for hot rolled Ti micro-alloyed steels. J Mater Process Technol 311:117810. https://doi.org/10.1016/j.jmatprotec.2022.117810
9. Thomas A, Durmaz AR, Alam M, Gumbsch P, Sack H, Eberl C (2023) Materials fatigue prediction using graph neural networks on microstructure representations. Scientif Re13(1):12562 https://doi.org/10.1038/s41598-023-39400-2
10. Channi H.K, Kumar R.: Machine learning for metal additive manufacturing process optimization. In: Machine Learning for Powder-Based Metal Additive Manufacturing pp. 131–153. Elsevier. https://doi.org/10.1016/B978-0-443-22145-3.00006-2
11. Srivastava N, Singh AK, Arora A (2025) Overview of machine learning for additive manufacturing. In: Machine learning for powder-based metal additive manufacturing, Elsevier, pp 1–19 . https://doi.org/10.1016/B978-0-443-22145-3.00001-3
12. Stergiou K, Ntakolia C, Varytis P, Koumoulos E, Karlsson P, Moustakidis S (2023) Enhancing property prediction and process optimization in building materials through machine learning: A review. Comput Mater Sci 220:112031. https://doi.org/10.1016/j.commatsci.2023.112031
13. Bhat A, Gupta V, Aulakh SS, Elsen RS (2023) Generative design and analysis of a double-wishbone suspension assembly: A methodology for developing constraint oriented solutions for optimum material distribution. J Eng Des Technol 21(3):927–942. https://doi.org/10.1108/JEDT-06-2021-0293
14. Zhou Y, Dowsey M, Spelman T, Choong P, Schilling C (2023) Smart choice (knee) tool: A patient-focused predictive model to predict improvement in health-related quality of life after total knee arthroplasty. ANZ J Surg 93(1–2):316–327. https://doi.org/10.1111/ans.18250
15. Fine TL (2013) Feedforward neural network methodology. Springer. https://doi-org.ezproxy.biblio.polito.it/10.1007/b97705
16. Wu D, Jennings C, Terpenny J, Gao RX, Kumara S (2017) A comparative study on machine learning algorithms for smart manufacturing: Tool wear prediction using random forests. J Manuf Sci Eng 139(7):071018. https://doi.org/10.1115/1.4036350
17. Mahmood MA, Wu SH, Liou F, Ishfaq K (2025) Machine learning for design in additive manufacturing. In: Machine learning for

powder-based metal additive manufacturing, Elsevier, pp 21–42. https://doi.org/10.1016/B978-0-443-22145-3.00002-5.
18. Salam MA, Taher A, Samy M, Mohamed K () The effect of different dimensionality reduction techniques on machine learning overfitting problem. Int J Adv Comput Sci Appl 12(4). https://doi.org/10.14569/IJACSA.2021.0120480
19. Batu T, Lemu HG, Shimels H (2023) Application of artificial intelligence for surface roughness prediction of additively manufactured components. 16(18):6266. https://doi.org/10.3390/ma16186266
20. Muhammad W, Kang J, Ibragimova O, Inal K (2023) Experimental investigation and development of a deep learning framework to predict process-induced surface roughness in additively manufactured aluminum alloys. 67(4):897–921. https://doi.org/10.1007/s40194-022-01445-8
21. Alamri F, Barsoum I, Bojanampati S, Maalouf M (2025) Prediction of porosity, hardness and surface roughness in additive manufactured AlSi10Mg samples. 20(3):0316600. https://doi.org/10.1371/journal.pone.0316600
22. Koo J, Lee S, Baek AMC, Park E, Kim N (2024) Downskin surface roughness prediction with machine learning for as-built CM247LC fabricated via powder bed fusion with a laser beam. 11(4):1510–1522. https://doi.org/10.1089/3dp.2022.0365
23. Islahudin N, Nugroho DS, Wijaya DK, Amalia Suprijono H, Ginta TL, Azka M, Rahadian H (2025) Machine learning-driven optimization for surface roughness prediction of vertical orientation measurements on 3D printed components. 28:101046. https://doi.org/10.1016/j.clet.2025.101046
24. Wang D, Liu Y, Yang Y, Xiao D (2016) Theoretical and experimental study on surface roughness of 316L stainless steel metal parts obtained through selective laser melting. 22(4):706–716. https://doi.org/10.1108/RPJ-06-2015-0078
25. Balbaa MA, Elbestawi MA, McIsaac J (2019) An experimental investigation of surface integrity in selective laser melting of Inconel 625. 104(9-12):3511–3529. https://doi.org/10.1007/s00170-019-03949-y
26. Yusuf SM, Gao N (2017) Influence of energy density on metallurgy and properties in metal additive manufacturing. 33(11):1269–1289 https://doi.org/10.1080/02670836.2017.1289444
27. Qu S, Ding J, Fu J, Fu M, Zhang B, Song X (2021a) High-precision laser powder bed fusion processing of pure copper. 48:102417. https://doi.org/10.1016/j.addma.2021.102417
28. Abdelhafiz M, Al-Rubaie K., Emadi A, Elbestawi MA (2021) Process–structure–property relationships of copper parts manufactured by laser powder bed fusion. 14(11):2945. https://doi.org/10.3390/ma14112945
29. Yan X, Chang C, Dong D, Gao S, Ma W, Liu M, Liao H, Yin S (2020) Microstructure and mechanical properties of pure copper manufactured by selective laser melting. 789:139615. https://doi.org/10.1016/j.msea.2020.139615
30. Ullah A, Ur Rehman A, Salamci MU, Pıtır F, Liu T (2022) The influence of laser power and scanning speed on the microstructure and surface morphology of Cu2O parts in SLM. 28(9):1796–1807. https://doi.org/10.1108/RPJ-12-2021-0342
31. Murugesan SK, Natarajan J, Yang CH, Vijayananth K (2023) A synergistic impact of LPBF process parameters on attaining a defect-free Cu-Cr-Zr alloy parts: An analytical and experimental study. 128(7-8):3507–3529. https://doi.org/10.1007/s00170-023-12179-2
32. Balbaa M, Mekhiel S, Elbestawi M, McIsaac J (2020) On selective laser melting of Inconel 718: Densification surface roughness and residual stresses. 193:108818. https://doi.org/10.1016/j.matdes.2020.108818
33. Hu R, Su K, Lao Z, Cai Y, Fu B, Yuen MMF, Gao Z, Cao M, Wang Y (2023) Process of pure copper fabricated by selective laser melting (SLM) technology under moderate laser power with re-melting strategy. 16(7):2642. https://doi.org/10.3390/ma16072642
34. Ulbricht A, Altenburg SJ, Sprengel M, Sommer K, Mohr G, Fritsch T, Mishurova T, Serrano-Munoz I, Evans A, Hofmann M, Bruno G (2020) Separation of the formation mechanisms of residual stresses in LPBF 316L. Met 10(9):1234. https://doi.org/10.3390/met10091234
35. Serrano-Munoz I, Mishurova T, Thiede T, Sprengel M, Kromm A., Nadammal N, Nolze G, Saliwan-Neumann R, Evans A, Bruno G (2020) The residual stress in as-built laser powder bed fusion IN718 alloy as a consequence of the scanning strategy induced microstructure. Sci Rep 10(1):14645. https://doi.org/10.1038/s41598-020-71112-9
36. Crachi M, Sesana R, Delprete C, Pizzarelli M, Pavese M, Sicignano, N, Borrelli D (2025a) Experimental characterization of a new L-PBF AM 65% copper - 35% maraging steel metal-matrix-composite for liquid rocket engine thrust chambers. 45:112146. https://doi.org/10.1016/j.mtcomm.2025.112146
37. Lusicini D, Crachi M, Sesana R, Delprete C, Sicignano N (2025a) Experimental analysis of thermomechanical properties of innovative heat treated metal matrix composites processed by additive manufacturing for space rocket applications. 34(17):19824–19839. https://doi.org/10.1007/s11665-025-11165-x
38. Crachi M, Lusicini D, Sesana R, Delprete C, Pizzarelli M, Sicignano N, Borrelli D, Caraviello A (2025) Effect of LPBF process parameters on thermomechanical properties of a copper-based metal matrix composite. 147(10):101009. https://doi.org/10.1115/1.4069275
39. Fitnet. https://it.mathworks.com/help/deeplearning/ref/fitnet.html?searchHighlight=fitnet&s_tid=srchtitle_support_results_1_fitnet
40. mapminmax. https://it.mathworks.com/help/deeplearning/ref/mapminmax.html
41. Sinsomboonthong S (2022) Performance comparison of new adjusted min-max with decimal scaling and statistical column normalization methods for artificial neural network classification. 2022:1–9. https://doi.org/10.1155/2022/3584406
42. Chepino BG, Yacoub RR, Aula A, Saleh M, Sanjaya BW (2023) Effect of minmax normalization on orb data for improved ann accuracy. 11(2):29. https://doi.org/10.26418/j3eit.v11i2.68689
43. Nawi NM, Atomi WH, Rehman MZ (2013) The effect of data pre-processing on optimized training of artificial neural networks. 11:32–39. https://doi.org/10.1016/j.protcy.2013.12.159
44. Sikder R (2024) Rilevamento di intrusioni in tempo reale mediante video di sorveglianza a bassa risoluzione e riconoscimento facciale. https://amslaurea.unibo.it/id/eprint/31501/
45. Ramadevi B, Kasi VR, Bingi K (2024) Fractional ordering of activation functions for neural networks: A case study on texas wind turbine. Eng Appl Artif Intell 127:107308. https://doi.org/10.1016/j.engappai.2023.107308
46. Igwe KC, Oyedum OD, Aibinu AM, Ajewole MO, Moses AS (2021) Application of artificial neural network modeling techniques to signal strength computation. 7(3):06047. https://doi.org/10.1016/j.heliyon.2021.e06047
47. Tyagi K, Rane C, Harshvardhan Manry M (2022) Chapter 4 - regression analysis. In: Pandey R, Khatri SK, Singh N, Verma P (eds) Artificial intelligence and machine learning for EDGE computing, Academic Press, pp. 53–63. https://doi.org/10.1016/B978-0-12-824054-0.00007-1
48. Trainlm. https://it.mathworks.com/help/deeplearning/ref/trainlm.html
49. Rubio JDJ (2021) Stability analysis of the modified levenberg–marquardt algorithm for the artificial neural network training. IEEE Trans Neural Netw Learn Syst 32(8):3510–3524. https://doi.org/10.1109/TNNLS.2020.3015200

50. Uwimana E, Zhou Y, Sall NM (2025) A short-term load demand forecasting: Levenberg–Marquardt (LM) Bayesian regularization (BR), and scaled conjugate gradient (SCG) optimization algorithm analysis. The Journal of Supercomputing. 81(1):55. https://doi.org/10.1007/s11227-024-06513-y
51. Trainbr. https://it.mathworks.com/help/deeplearning/ref/trainbr.html
52. Kayri M (2016) Predictive Abilities of Bayesian regularization and levenberg–marquardt algorithms in artificial neural networks: A comparative empirical study on social data. Mathe Comput Appl 21(2):20. https://doi.org/10.3390/mca21020020
53. Trainbfg. https://it.mathworks.com/help/deeplearning/ref/trainbfg.html
54. Najmeddine A, Shakiba M (2024) Efficient BFGS quasi-Newton method for large deformation phase-field modeling of fracture in hyperelastic materials. Eng Fract Mech 310:110463. https://doi.org/10.1016/j.engfracmech.2024.110463
55. Trainrp. https://it.mathworks.com/help/deeplearning/ref/trainrp.html
56. Lin Q, Leandro J, Gerber S, Disse M (2020) Multistep flood inundation forecasts with resilient backpropagation neural networks: Kulmbach case study. Water 12(12):3568. https://doi.org/10.3390/w12123568
57. Trainscg. https://it.mathworks.com/help/deeplearning/ref/trainscg.html
58. Traincgb. https://it.mathworks.com/help/deeplearning/ref/traincgb.html
59. Traincgf. https://it.mathworks.com/help/deeplearning/ref/traincgf.html
60. Traincgp. https://it.mathworks.com/help/deeplearning/ref/traincgp.html
61. Trainoss. https://it.mathworks.com/help/deeplearning/ref/trainoss.html
62. Nguyen QH, Ly HB, Tran VQ, Nguyen TA, Phan VH, Le TT, Pham BT (2020) A novel hybrid model based on a feedforward neural network and one step secant algorithm for prediction of load-bearing capacity of rectangular concrete-filled steel tube columns. Mol 25(15). https://doi.org/10.3390/molecules25153486
63. Traingdx. https://it.mathworks.com/help/deeplearning/ref/traingdx.html
64. Lu Y, Li W, Wang H (2020) A batch variable learning rate gradient descent algorithm with the smoothing l1/2 regularization for takagi-sugeno models. IEEE Access 8:100185–100193. https://doi.org/10.1109/ACCESS.2020.2997867
65. Traingdm. https://it.mathworks.com/help/deeplearning/ref/traingdm.html
66. Gong X, Ding X (2021) Adaptive cdkf based on gradient descent with momentum and its application to pos. IEEE Sens J 21(14):16201–16212. https://doi.org/10.1109/JSEN.2021.3076071
67. Traingd. https://it.mathworks.com/help/deeplearning/ref/traingd.html
68. Hong WK (2023) 4 - forward and backpropagation for artificial neural networks. In: Hong WK (ed) Artificial intelligence-based design of reinforced concrete structures. woodhead publishing series in civil and structural engineering, Woodhead Publishing, pp 67–116. https://doi.org/10.1016/B978-0-443-15252-8.00006-6
69. Özel T, Altay A, Kaftanoğlu B, Leach R, Senin N, Donmez A (2020) Focus variation measurement and prediction of surface texture parameters using machine learning in laser powder bed fusion. J Manuf Sci Eng 142(1):011008. https://doi.org/10.1115/1.4045415
70. Wu Q, Wang X, Yan B, Luo S, Zheng X, Tan L, Zhu W (2024) Prediction of impact sensitivity and electrostatic spark sensitivity for energetic compounds by machine learning and density functional theory. J Mater Sci 59(20):8894–8910. https://doi.org/10.1007/s10853-024-09742-x
71. Xia C, Pan Z, Polden J, Li H, Xu Y, Chen S (2022) Modelling and prediction of surface roughness in wire arc additive manufacturing using machine learning. J Intell Manuf 33(5):1467–1482. https://doi.org/10.1007/s10845-020-01725-4
72. Kushwaha R, Singh MK, Krishnan S, Rai DK (2023) Machine learning enabled property prediction of carbon-based electrodes for supercapacitors. J Mater Sci 58(39):15448–15458. https://doi.org/10.1007/s10853-023-08981-8
73. Fu T, Tang X, Cai Z, Zuo Y, Tang Y, Zhao X (2020) Correlation research of phase angle variation and coating performance by means of Pearson's correlation coefficient. Progr Org Coat 139:105459. https://doi.org/10.1016/j.porgcoat.2019.105459
74. Molnar C (2022) Interpretable machine learning: A guide for making black box models explainable . https://christophm.github.io/interpretable-ml-book/
75. Fisher A, Rudin C, Dominici F (2021) All models are wrong but many are useful: Learning a variable's importance by studying an entire class of prediction models simultaneously
76. Molnar C, Freiesleben T, König G, Herbinger J, Reisinger T, Casalicchio G, Wright MN, Bischl B (2023) Relating the partial dependence plot and permutation feature importance to the data generating process. In: Longo L (ed) Explainable artificial intelligence, Springer Cham, pp 456–479
77. fmincon. https://it.mathworks.com/help/optim/ug/fmincon.html
78. Nocedal J, Wright SJ (1999) Numerical optimization. Springer series in operations research. Springer
79. Jakšić O, Jakšić Z, Guha K, Silva AG, Laskar NM (2023) Comparing artificial neural network algorithms for prediction of higher heating value for different types of biomass. Soft Comput 27(9):5933–5950. https://doi.org/10.1007/s00500-022-07641-4
80. Zhang T, Yuan L (2024) Interaction of contour and hatch parameters on vertical surface roughness in laser powder bed fusion. J Mater Res Technol 32:3390–3401. https://doi.org/10.1016/j.jmrt.2024.08.170
81. Alwosheel A, Van Cranenburgh S, Chorus CG (2018) Is your dataset big enough? Sample size requirements when using artificial neural networks for discrete choice analysis. 28:167–182. https://doi.org/10.1016/j.jocm.2018.07.002